

# Imaging the Ice Sheet and Uppermost Crustal Structures with a Dense Linear Seismic Array in the Larsemann Hills, Prydz Bay, East Antarctica

Lei Fu<sup>1,2</sup>, Jingxue Guo<sup>3</sup>, Junlun Li<sup>4</sup>, Bao Deng<sup>4</sup>, Guofeng Liu<sup>5</sup>, Enzhao Xiao<sup>3</sup>, and Xiaofei Chen<sup>\*1,2</sup>

## Abstract

Comprehensive geophysical surveys including magnetotelluric, seismic, and aerial gravity–magnetic surveys are essential for understanding the history of Antarctic tectonics. The ice sheet and uppermost structure derived from those geophysical methods are relatively low resolution. Although ice-penetrating radar can provide high-resolution reflectivity images of the ice sheet, it cannot provide constraints on subice physical properties, which are important for geological understanding of the Antarctic continent. To obtain high-resolution images of the ice sheet and uppermost crustal structure beneath the Larsemann Hills, Prydz Bay, East Antarctica, we conduct an ambient noise seismic experiment with 100 short-period seismometers spaced at 0.2 km intervals. Continuous seismic waveforms are recorded for one month at a 2 ms sampling rate. Empirical Green's functions are extracted by cross correlating the seismic waveform of one station with that of another station, and dispersion curves are extracted using a new phase-shift method. A high-resolution shear-velocity model is derived by inverting the dispersion curves. Furthermore, body waves are enhanced using a set of processing techniques commonly used in seismic exploration. The stacked body-wave image clearly shows a geological structure similar to that revealed by the shear-wave velocity model. This study, which is the first of its kind in Antarctica, possibly reveals a near-vertical intrusive rock covered by an ice sheet with a horizontal extent of 4 km. Our results help to improve the understanding of the subice environment and geological evolution in the Larsemann Hills, Prydz Bay, East Antarctica.

**Cite this article as** Fu, L., J. Guo, J. Li, B. Deng, G. Liu, E. Xiao, and X. Chen (2021). Imaging the Ice Sheet and Uppermost Crustal Structures with a Dense Linear Seismic Array in the Larsemann Hills, Prydz Bay, East Antarctica, *Seismol. Res. Lett.* **93**, 288–295, doi: [10.1785/0220210135](https://doi.org/10.1785/0220210135).

[Supplemental Material](#)

## Introduction

Geologic research on the Antarctica continent holds great significance for understanding the evolution of the Earth's lithosphere (Yoshida *et al.*, 1992; Fitzsimons, 2000; Liu *et al.*, 2007; Boger, 2011). Geologically, Antarctica can be divided into two major tectonic units, namely, the East Antarctica shield and the West Antarctica Phanerozoic active zone (Fitzsimons, 2000). The late Neoproterozoic–early Paleozoic tectonic thermal events in East Antarctica and their role and significance in the assembly process of the Gondwana supercontinent (Unrug, 1997; Kemp *et al.*, 2006) are the frontiers and hotspots of international geoscience research. The Prydz orogenic belt (Boger *et al.*, 2001) is mainly exposed in Prydz Bay and Denman Glacier (Black *et al.*, 1992). There are two different understandings of the causes of the Prydz orogenic belt: collision orogen (Hensen and Zhou, 1997; Boger *et al.*, 2001; Zhao *et al.*, 2003) and intraplate transformation (Yoshida, 1995; Wilson *et al.*, 1997). The reason is that the Prydz orogenic belt

is located inside the previously assumed unified East Gondwana block and lack high-pressure metamorphic rocks related to oceanic plate subduction. In addition, the internal composition, structure, and extension direction of the Prydz orogenic belt are unclear (Liu *et al.*, 2007).

Less than 2% of Antarctica's surface contains exposed rock outcrops, limiting our understanding of Antarctica's tectonic evolution. Comprehensive geophysical surveys including

1. Department of Earth and Space Sciences, Southern University of Science and Technology, Shenzhen, China, <https://orcid.org/0000-0002-0950-8121> (XC); 2. Southern Marine Science and Engineering Guangdong Laboratory (Guangzhou), Guangzhou, China; 3. Key Laboratory for Polar Science, MNR, Polar Research Institute of China, Shanghai, China, <https://orcid.org/0000-0001-7761-8819> (JG); <https://orcid.org/0000-0003-3338-2423> (EX); 4. School of Earth and Space Sciences, University of Science and Technology of China, Hefei, China; 5. School of Geophysics and Information Technology, China University of Geosciences (Beijing), Beijing, China

\*Corresponding author: [chenxf@sustech.edu.cn](mailto:chenxf@sustech.edu.cn)

© Seismological Society of America

magnetotelluric (Beblo and Liebig, 1990; Wannamaker *et al.*, 2004), deep seismic sounding (Janik *et al.*, 2014), and surface-wave imaging (Knopoff and Vane, 1978; Danesi and Morelli, 2001; Ritzwoller *et al.*, 2001; Lawrence *et al.*, 2006) are essential for understanding Antarctic tectonics. For example, An *et al.* (2015) built a 3D S-velocity model for the Antarctic lithosphere using a single-step surface-wave tomographic method with seismic records from 122 broadband seismic stations, and the very thick crust beneath the East Antarctic Mountain Range may represent the collision suture of East Gondwana with Indo-Antarctica and West Gondwana during the Pan-African orogeny.

With the emergence and development of ambient noise technology (Shapiro *et al.*, 2005; Yao *et al.*, 2006, 2008), the ambient noise recorded by broadband seismic stations can be used to image subsurface structures. Ambient noise technology uses cross correlation to calculate the empirical Green's function (EGF) between pairs of stations and then generates tomographic images or dispersion-curve inversions to obtain the corresponding shear-wave velocity structure. Zhan *et al.* (2014) studied noise cross correlations and autocorrelations on the Amery Ice Shelf and obtained an independent estimate of the water column thickness. Diez *et al.* (2016) analyzed the ice-shelf structure by inverting dispersion curves from ambient noise in the Ross Ice Shelf. Yan *et al.* (2018) estimated ice-sheet thickness using the horizontal-to-vertical spectral ratio (HVSr) method with single-station seismic ambient noise in Antarctica. O'Donnell *et al.* (2019) obtained a 3D shear-wave velocity model and estimated the radial anisotropy in West Antarctica crust from 8- to 25-s-period Rayleigh- and Love-wave phase velocity dispersion data extracted from seismic ambient noise.

Broadband seismographs are expensive and difficult to deploy on the Antarctic continent. Furthermore, the distance between broadband stations is usually tens of kilometers; therefore, obtaining high-resolution lithospheric images beneath the ice sheet using limited seismic data from broadband stations is impossible. Recently, with the advancement of observation technology, dense seismic arrays have provided new options for obtaining high-resolution images of lithospheric structures. For example, Lin *et al.* (2013) derived a high-resolution near-surface shear-wave velocity model for Long Beach, U.S.A., using 5200 short-period stations with an average spacing of 100 m. Z. Liu *et al.* (2017) obtained new images of the crustal structure beneath eastern Tibet from a high-density seismic array with 330 short-period seismographs spaced at 500 m intervals.

In the past five austral seasons, the Polar Research Institute of China acquired aerial gravity-magnetic and ice-penetrating radar data in the Larsemann Hills with Snow Eagle 601 (Cui, Greenbaum, *et al.*, 2020). However, the resolution of the crustal structure derived from aerial gravity-magnetic data is relatively low. Although ice-penetrating radar can produce high-

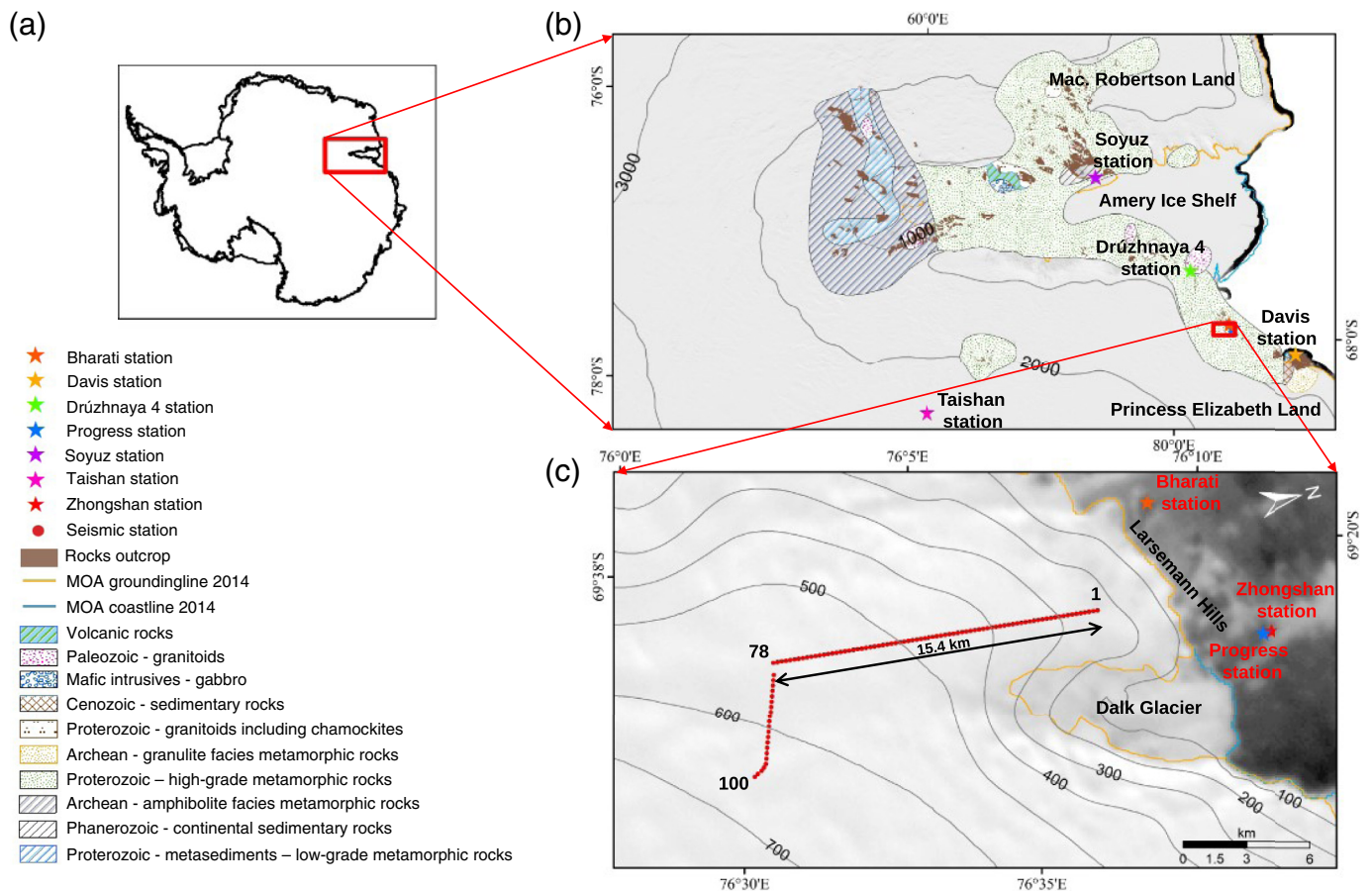
resolution images of ice sheets (Cui, Jeofry, *et al.*, 2020), it cannot provide the physical properties of subice material that are important for geological research in Prydz Bay. To obtain high-resolution images of the geologic structures within the ice sheet and the uppermost crust in the Larsemann Hills, we carry out a seismic experiment in the Larsemann Hills, during the 36th Chinese National Antarctic Research Expedition (CHINARE36). Stacked body-wave images and inverted shear-wave velocity model reveal the geologic structure of the ice sheet and the uppermost crust beneath the survey line, which provides the first high-resolution seismic evidence for widespread intrusive rocks covered by ice sheets in the Prydz orogenic belt, East Antarctica.

## Geological Setting

The basement of the Antarctic continent was formed during the Proterozoic. The central part of the Delonging-Maud continent in eastern Antarctica is mainly composed of high-grade metamorphic rocks. These metamorphic rocks are intruded by igneous rocks, forming coastal and inland mountain outcrops (Dallmann *et al.*, 1990). Studies from Grove Mountain and Prince Charles Mountain (X. Liu *et al.*, 2017) show that intrusive rocks from the Pan-African event are widely present in East Antarctica and represent the impact of the Prydz orogen on this region. The formation of the Larsemann Hills, Princess Elizabeth Land, and MacRobertson Land had important influences on the formation of subglacial tectonics (Sun *et al.*, 2009, 2014; Cui *et al.*, 2015; Cui, Jeofry, *et al.*, 2020). The study area shown in Figure 1c is located on the Westodon Peninsula in the Larsemann Hills region of Prydz Bay, Princess Elizabeth Land, East Antarctica. It is dominated by Quaternary glacial meltwater deposits, metamorphic rocks, and intrusive rocks according to limited outcrops. The representative lithologies of metamorphic rocks are fine-grained massive gneiss, mafic granulite, felsic gneiss (some containing pyroxene), argillaceous-felsic gneiss (some containing magnetite), and garnet biotite quartz schist; intrusive rocks are mainly granite (Liu *et al.*, 2006, 2007). These representative rocks are an important component of the Grenville period in East Antarctica and for a long time were considered to represent only the orogenic products of the Grenville period (Harley *et al.*, 1998; Liu *et al.*, 2006).

## Data and Methods

During the CHINARE36 field seasons, we deployed 100 short-period, three-component seismometers (Fig. 1c), each with a corner frequency of 0.2 Hz, on the ice sheet in the Larsemann Hills. All seismometers were buried at a depth of one-half meter in the snow. A wooden stick was placed near the seismometer to assist with instrument retrieval, as the ice flow velocity was more than 10 m/a here. The first seismometer was located at the north end of the seismic survey line (Fig. 1c), and the interstation distance was 0.2 km, which resulted in a total survey length of 19.8 km. The seismic survey line turns



east at the 78th station because there are many crevasses toward the south. The sampling frequency was 500 Hz for all stations, and we recorded ambient seismic noise for one month. We focus on the straight-line section between stations 1–78 in this study. The raw vertical-component data were divided into one-day segments, and the preprocessing steps, including instrument response and trend removal as well as band-pass filtering, were applied to all segments. EGFs are calculated by correlating the preprocessed waveforms with those recorded at other stations. Figure 2a shows the raw virtual common shot gathers (CSGs; Draganov *et al.*, 2009) with the virtual shot position located at the first station. Figure 2b–d shows the band-pass-filtered CSGs with different filters. The red arrows represent the surface waves. We note that the body-wave reflections from shallow interfaces are contaminated by surface waves. Special processing steps are essential to enhance the body-wave reflections from subsurface interfaces.

### Retrieving the body-wave image

The energy of body waves is much weaker than that of surface waves, which results in invisibility by the naked eye. Several processing steps are needed to enhance the body waves. The first step is geometric spreading compensation (Červený *et al.*, 1974), which is mainly used to account for the energy dissipation of seismic-wave propagation with depth, so that the reflected energy at different depths is consistent. The second step is

**Figure 1.** (a) Antarctic map. (b) Portion geologic map of East Antarctic. The red box indicates the study area where the basement consists of Proterozoic high-grade metamorphic rocks. (c) Digital elevation map showing the location of the linear dense seismic array (red-dotted line) deployed in the Larsemann Hills. The color version of this figure is available only in the electronic edition.

denoising (Liu *et al.*, 2021), which transforms the data to different trace positions and removes strong surface waves and abnormal amplitudes. During this process, maintaining the energy integrity of the reflections in the frequency band is important. Figure 3b shows the denoised CSG, in which the energy of low-frequency (<10 Hz) surface waves is largely suppressed, and the energy of high-frequency (>10 Hz) body waves is enhanced; in contrast, the energy of the CSG in Figure 3a is dominated by the surface wave. The third step is to compensate for the uniform amplitude of the ground surface, so that the energy from different shots can reach the same level. The fourth step is deconvolution (Idier and Goussard, 1993), which mainly expands the frequency bandwidth of the seismic record and makes the source wavelets in the record consistent. The CSG after deconvolution is shown in Figure 3c, in which the reflections are clearly revealed in the area indicated by the red ellipse. The fifth step is to transform the data to the common midpoint domain,

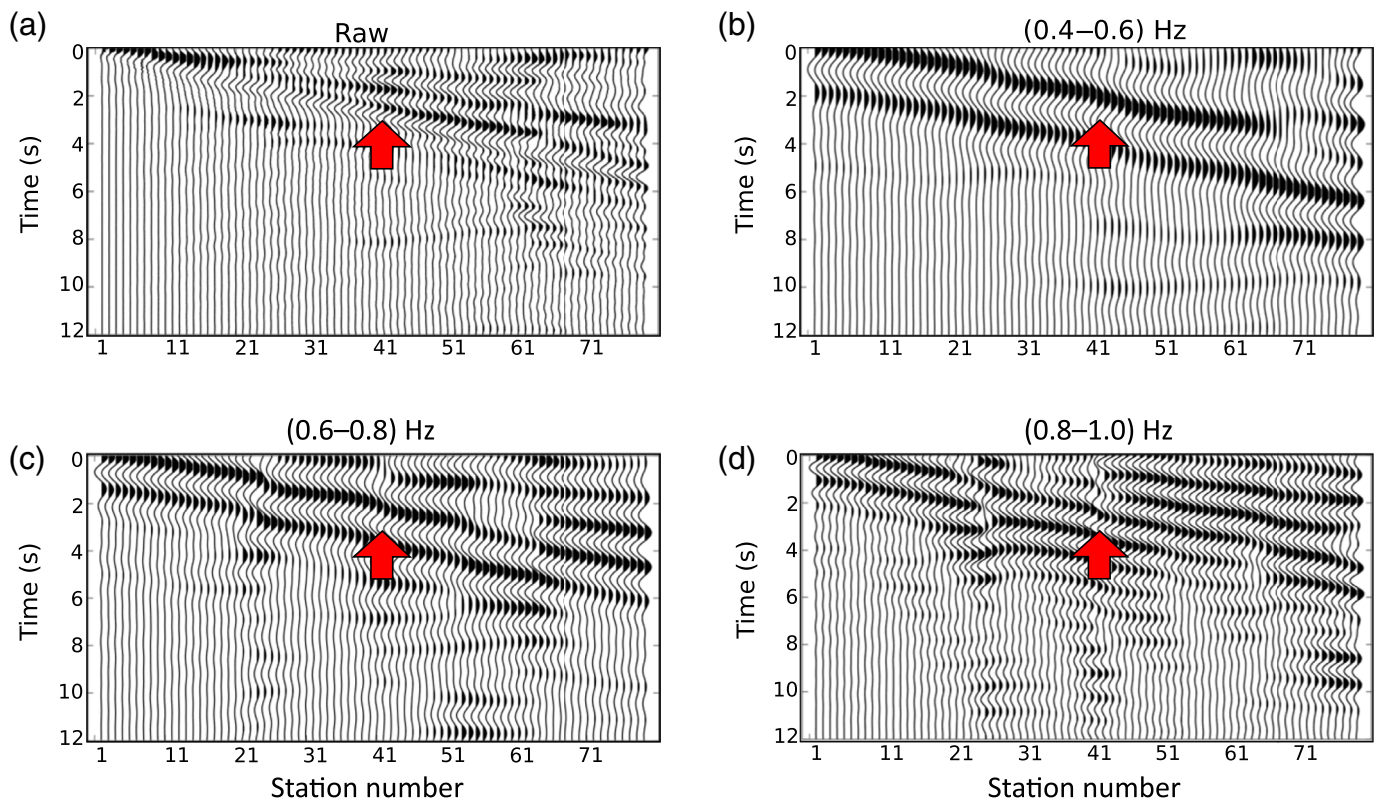


**Figure 2.** (a) Raw virtual common shot gather (CSG). CSGs filtered at (b) 0.4–0.6 Hz, (c) 0.6–0.8 Hz, and (d) 0.8–1.0 Hz. The virtual shot position is located at the first station; red arrows indicate surface waves. The color version of this figure is available only in the electronic edition.

perform velocity analysis (Wood *et al.*, 1994), and then use the velocity result for normal moveout correction (Dunkin and Levin, 1973). Finally, coherent in-phase reflections are enhanced by stacking. Figure S1a–c, available in the supplemental material to this article, shows the stacked images with the original, denoised, and deconvolutional CSGs, respectively. The body-wave reflections are enhanced in the final stacking image after the data-processing steps.

### Inversion of Rayleigh-wave dispersion curves

The extended range phase-shift (ERPS) method is used to extract broadband frequency dispersion curves. First, the internal-array phase shift and external-array phase shift are separately applied to measure the phase velocity at high and low frequencies. Then, we merge the two types of dispersion curves at an appropriate frequency band for each station. Therefore, broadband dispersion curves that have strong constraints from both shallow and deep structures are acquired, so that we can image the near-surface structure with high resolution. The phase velocity maps from 0.2 to 3 s derived by the ERPS method for the straight-line profile (stations 1–78) are shown in Figure S2. The low phase velocity in short period is about 1.6–2.0 km/s, which is related to the ice sheet, and the high phase velocity (>3 km/s) in long period is corresponding to the bedrock. A low-velocity anomaly between  $-69.55^\circ$  and  $-69.52^\circ$  latitude, from 0.5 to 1 s, is found in the phase velocity map.

Next, the obtained dispersion curves are used to simultaneously invert for the shear-wave velocity profile, as opposed to inverting them independently at each point (Feng and An, 2010). The shear-wave velocity ( $V_S$ ) model is estimated with an iteratively damped least-squares algorithm that adds vertical and horizontal constraints. This problem is linearized by a first-order Taylor expansion as follows:

$$G\delta m = \delta d, \quad (1)$$

in which  $G$  denotes the Jacobian matrix, elements of which represent the sensitivity of the phase velocity with respect to  $V_S$ ;  $\delta m$  denotes the difference between the current model and the true model; and  $\delta d$  denotes the misfit for the dispersion curves. To solve equation (1), second-order Tikhonov regularization is employed, and different damping parameters for the vertical and horizontal directions are selected. For the  $k$ th iteration, we obtain,

$$\delta m^k = (G^T G + \lambda_v L_v^T L_v + \lambda_h L_h^T L_h)^{-1} G^T \delta d, \quad (2)$$

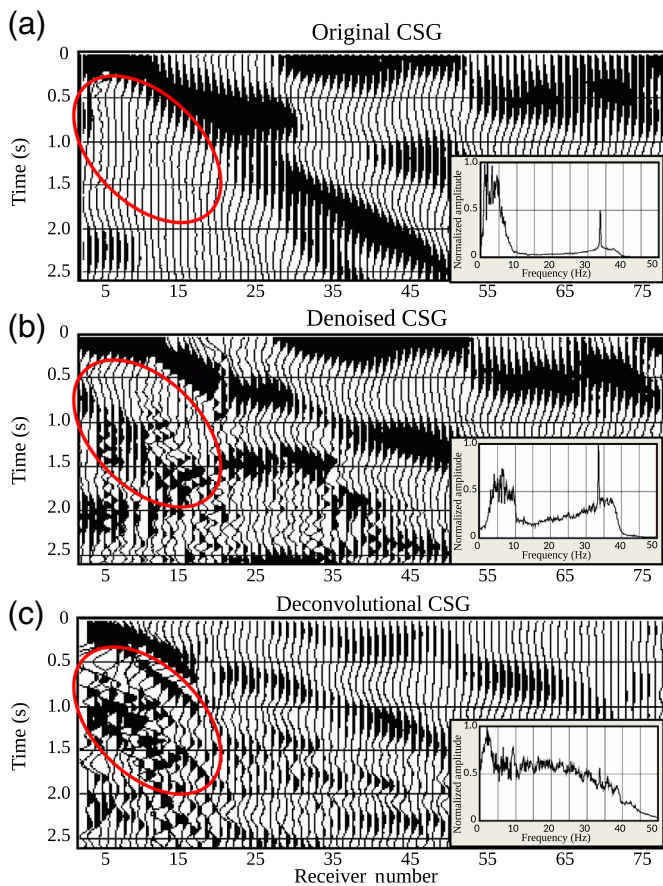


**Figure 3.** (a) Original virtual CSGs, (b) denoised CSG with surface wave suppressed, and (c) deconvolutional CSG, in which the reflections are clearly revealed in the area indicated by the red ellipse. The subplots in the lower-right panel are the average normalized magnitude spectrum. The color version of this figure is available only in the electronic edition.

in which  $\delta m^k$  denotes the adjustment to update the model;  $L_v$  and  $L_h$  are the vertical and horizontal Laplacian constraints, respectively; and  $\lambda_v$  and  $\lambda_h$  are the corresponding damping parameters.

## Results and Discussion

The body-wave stacking image is shown in Figure 4a. A clear arrival, indicated by the red arrow and associated curve, marks the reflection from the ice–rock interface. The estimated thickness of the ice sheet varies from 0.2 (in the north) to 0.5 km (in the south), which is consistent with the HVSr (Picotti *et al.*, 2017) estimates shown in Figure S3. Another clear arrival, identified by the black arrow and the purple curve in Figure 4a, indicates a subsurface geologic interface, and the thickness of this layer should be greater than 0.2 km. Our shear-wave velocity model is shown in Figure 4b. The maximum depth of the shear-wave velocity model shown in Figure 4 is less than 2.5 km, which is reasonable and reliable,

as the maximum period in our data is approximately 3 s, and the corresponding dominant wavelength is approximately 7.5 km, assuming the average shear velocity of 2.5 km/s. Therefore, we constrain the depth in the shear-wave velocity model to approximately 1/3 of the dominant wavelength. To obtain the high-resolution geologic structure at deeper depths, the aperture of the seismic survey line would need to be increased to capture low-frequency signals. Furthermore, the acquisition time of ambient noise recording should be increased.

The blue-purple section at shallow depths in Figure 4b is the ice sheet, in which the average shear-wave velocity is approximately 1.85 km/s, and the ice–rock interface is marked by the red curve. The average shear-wave velocity of the green area (between the red and purple curves) is approximately 2.9 km/s, whereas the average shear-wave velocity for the red section is approximately 3.6 km/s. In addition, we find a near-vertical low-velocity anomaly between  $-69.55^\circ$  and  $-69.52^\circ$  latitude, marked by the dashed-white line, with a horizontal extent of 4 km. The average shear-wave velocity of the anomaly is approximately 3.4 km/s.

Our geologic interpretation is shown in Figure 5. The average shear-wave velocity of ice sheet is approximately 1.85 km/s, which is close to that estimated by Wittlinger and Farra (2012). The ice shear-wave velocity increases from 1.6 km/s at the surface to 2.2 km/s at the base of the ice sheet; the velocity variations below the firn-ice transition zone are mostly due to crystal fabric (Kluskiwicz *et al.*, 2017). We infer that the yellow sections in Figure 5, with shear-wave velocity of  $\sim 3.6$  km/s, should correspond to high-grade metamorphic rocks, as the seismic survey line (Fig. 1) is located above the corresponding geologic unit. In addition, the shear-wave velocity for metamorphic rocks is typically high (Christensen, 1966). The red section in Figure 5 is interpreted as a granite intrusive rock with a horizontal extent of 4 km, possibly associated with Pan-African thermal events. The shear-wave velocity near the ice–rock interface is slightly lower than the average velocity (Hansen *et al.*, 2010). This may be because the granitic rocks have undergone weathering.

## Conclusions

A dense linear seismic array was deployed in the Larsemann Hills, East Antarctica, with a station spacing of 0.2 km. Continuous seismic waveforms were recorded for one month with a 2 ms sampling rate. Stacked body-wave images are extracted from EGFs from ambient noise using a set of processing techniques commonly employed in seismic exploration. In addition, dispersion curves are extracted from the EGFs using the extended phase-shift method, and a shear-wave velocity model is then generated by simultaneously inverting those dispersion curves. The shear-wave velocity model shows good agreement with the stacked body-wave image. Our results provide a high-resolution image of the seismic structure, in which

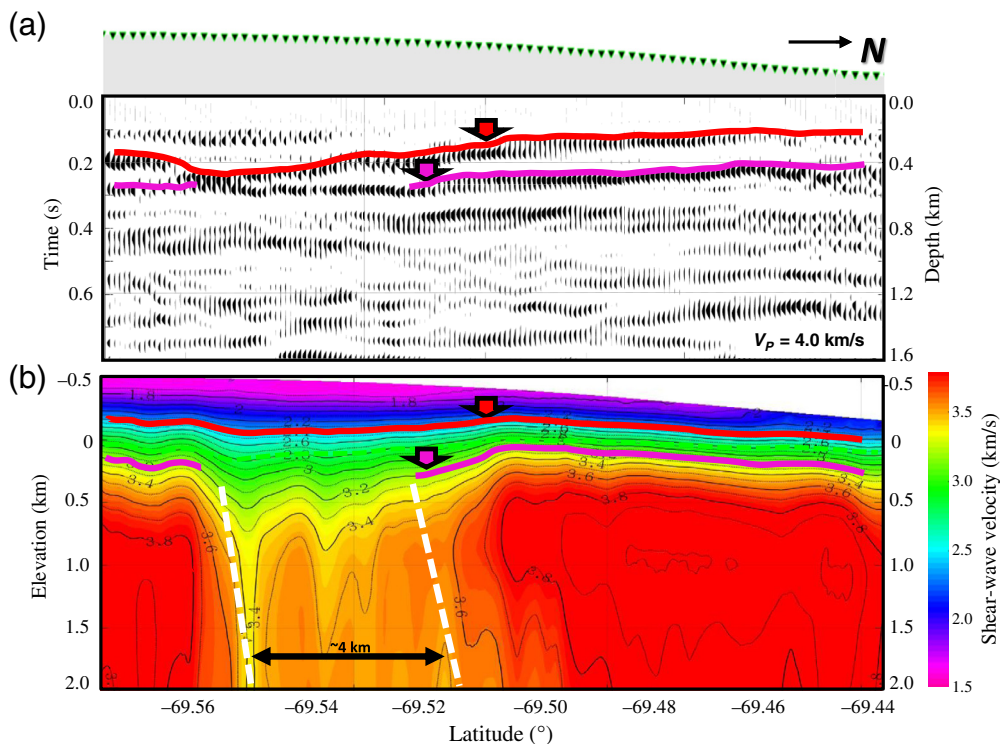


**Figure 4.** (a) Stacked body-wave image. The gray section on the top represents the ice sheet, in which the surface elevation changes from 0.2 to 0.5 km. Green triangles represent the seismic stations deployed on top of the ice sheet; (b) the shear-wave velocity model from the inversion of dispersion curves. The color version of this figure is available only in the electronic edition.

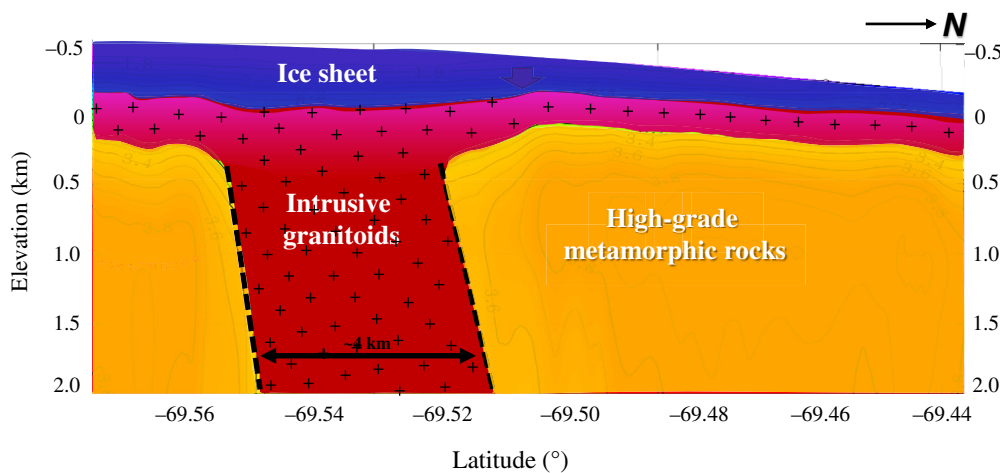


**Figure 5.** Geologic interpretation based on the results shown in Figure 4. The color version of this figure is available only in the electronic edition.

the ice sheet and subice geologic units are identified. A near-vertical intrusive rock anomaly with a horizontal extent of 4 km is found beneath the seismic survey line. These results provide the first high-resolution seismic evidence for

widespread intrusive rocks covered by ice sheets in the Prydz orogenic belt, East Antarctica. Our results may help improve the understanding of the subice environment and geologic evolution in the Larsemann Hills, Prydz Bay, East Antarctica.

## Data and Resources

The raw ambient noise data used in this study are archived on the Harvard Dataverse website (DOI: [10.7910/DVN/GXJ6VH](https://doi.org/10.7910/DVN/GXJ6VH)). The supplemental material for this article includes (1) the stacked body-wave images, (2) phase velocity maps derived from the extended range phase-shift method for the straight profile, and (3) peak frequencies and corresponding ice thickness derived from horizontal-to-vertical spectral ratio (HVSr) method.

## Declaration of Competing Interests

The authors acknowledge that there are no conflicts of interest recorded.

## Acknowledgments

The authors are grateful to Meijian An from the Chinese Academy of Geological Sciences, and Gang Qiao and Yanjun Li from Tongji University for helpful discussions that improved the original article. The authors also thank the two reviewers for their constructive comments. This research is supported by the National Natural Science Foundation of China (Grant Numbers 41974044, U1901602, 41790465, and 41876227) and the National Key Research and Development Projects (2018YFC0603500).

Finally, the authors acknowledge the support of Shenzhen Key Laboratory of Deep Offshore Oil and Gas Exploration Technology (Grant Number ZDSYS20190902093007855), Leading Talents of Guangdong Province Program (Grant Number 2016LJ06N652), Key Special Project for Introduced Talents Team of Southern Marine

Science and Engineering Guangdong Laboratory (Guangzhou) (GML2019ZD0203), and Shenzhen Science and Technology Program (Grant Number KQTD20170810111725321).

## References

- An, M., D. A. Wiens, Y. Zhao, M. Feng, A. A. Nyblade, M. Kanao, Y. Li, A. Maggi, and J. J. L ev eque (2015). S-velocity model and inferred Moho topography beneath the Antarctic plate from Rayleigh waves, *J. Geophys. Res.* **120**, no. 1, 359–383.
- Beblo, M., and V. Liebig (1990). Magnetotelluric measurements in Antarctica, *Phys. Earth Planet. In.* **60**, nos. 1/4, 89–99.
- Black, L. P., J. W. Sheraton, R. J. Tingey, and M. T. McCulloch (1992). New U–Pb zircon ages from the Denman Glacier area, East Antarctica, and their significance for Gondwana reconstruction, *Antarct. Sci.* **4**, no. 4, 447–460.
- Boger, S. D. (2011). Antarctica—Before and after Gondwana, *Gondwana Res.* **19**, no. 2, 335–371.
- Boger, S. D., C. J. L. Wilson, and C. M. Fanning (2001). Early Paleozoic tectonism within the East Antarctic craton: The final suture between east and west Gondwana? *Geology* **29**, no. 5, 463–466.
- Christensen, N. I. (1966). Shear wave velocities in metamorphic rocks at pressures to 10 kilobars, *J. Geophys. Res.* **71**, no. 14, 3549–3556.
- Cui, X., J. S. Greenbaum, S. Lang, X. Zhao, L. Li, J. Guo, and B. Sun (2020). The scientific operations of Snow Eagle 601 in Antarctica in the past five austral seasons, *Remote Sens.* **12**, no. 18, 2994, doi: [10.3390/rs12182994](https://doi.org/10.3390/rs12182994).
- Cui, X., H. Jeofry, J. S. Greenbaum, J. Guo, L. Li, L. E. Lindzey, F. A. Habbal, W. Wei, D. A. Young, N. Ross, et al. (2020). Bed topography of Princess Elizabeth Land in East Antarctica, *Earth Syst. Sci. Data* **12**, no. 4, 2765–2774.
- Cui, X., B. Sun, J. Guo, T. Wang, and D. Zhang (2015). A new detailed ice thickness and subglacial topography DEM for Dome A, East Antarctica, *Polar Sci.* **9**, no. 4, 354–358.
- Červený, V., J. Langer, and I. Pšenčík (1974). Computation of geometric spreading of seismic body waves in laterally inhomogeneous media with curved interfaces, *Geophys. J. Int.* **38**, no. 1, 9–19.
- Danesi, S., and A. Morelli (2001). Structure of the upper mantle under the Antarctic plate from surface wave tomography, *Geophys. Res. Lett.* **28**, no. 23, 4395–4398.
- Diez, A., P. D. Bromirski, P. Gerstoft, R. A. Stephen, R. E. Anthony, R. C. Aster, C. Cai, A. Nyblade, and D. A. Wiens (2016). Ice shelf structure derived from dispersion curve analysis of ambient seismic noise, Ross Ice Shelf, Antarctica, *Geophys. J. Int.* **205**, no. 2, 785–795.
- Draganov, D., X. Campman, J. Thorbecke, A. Verdel, and K. Wapenaar (2009). Reflection images from ambient seismic noise, *Geophysics* **74**, no. 5, A63–A67.
- Dunkin, J. W., and F. K. Levin (1973). Effect of normal moveout on a seismic pulse, *Geophysics* **38**, no. 4, 635–642.
- Feng, M., and M. An (2010). Lithospheric structure of the Chinese mainland determined from joint inversion of regional and teleseismic Rayleigh-wave group velocities, *J. Geophys. Res.* **115**, no. B6, doi: [10.1029/2008JB005787](https://doi.org/10.1029/2008JB005787).
- Fitzsimons, I. C. W. (2000). A review of tectonic events in the East Antarctic shield and their implications for Gondwana and earlier supercontinents, *J. Afr. Earth Sci.* **31**, no. 1, 3–23.
- Hansen, S. E., A. A. Nyblade, D. S. Heeszel, D. A. Wiens, P. Shore, and M. Kanao (2010). Crustal structure of the Gamburtsev Mountains, East Antarctica, from S-wave receiver functions and Rayleigh wave phase velocities, *Earth Planet. Sci. Lett.* **300**, nos. 3/4, 395–401.
- Harley, S. L., I. Snape, and L. P. Black (1998). The evolution of a layered metaigneous complex in the Rauer Group, East Antarctica: Evidence for a distinct Archaean terrane, *Precambrian Res.* **89**, nos. 3/4, 175–205.
- Hensen, B. J., and B. Zhou (1997). East Gondwana amalgamation by Pan-African collision? Evidence from Prydz Bay, East Antarctica, In *The Antarctic Region: Geological Evolution and Processes*, C. A. Ricci (Editor), Terra Antarctica, Siena, Italy, 115–119.
- Idier, J., and Y. Goussard (1993). Multichannel seismic deconvolution, *IEEE Trans. Geosci. Remote Sens.* **31**, no. 5, 961–979.
- Janik, T., M. Grad, A. Guterch, and P. Środa (2014). The deep seismic structure of the Earth’s crust along the Antarctic Peninsula—A summary of the results from Polish geodynamical expeditions, *Glob. Planet. Change* **123**, 213–222.
- Kemp, A. I. S., C. J. Hawkesworth, B. A. Paterson, and P. D. Kinny (2006). Episodic growth of the Gondwana supercontinent from hafnium and oxygen isotopes in zircon, *Nature* **439**, no. 7076, 580–583.
- Kluskievicz, D., E. D. Waddington, S. Anandakrishnan, D. E. Voigt, K. Matsuoka, and M. P. McCarthy (2017). Sonic methods for measuring crystal orientation fabric in ice, and results from the West Antarctic ice sheet (WAIS) Divide, *J. Glaciol.* **63**, no. 240, 603–617.
- Knopoff, L., and G. Vane (1978). Age of East Antarctica from surface wave dispersion, *Pure Appl. Geophys.* **117**, no. 4, 806–815.
- Lawrence, J. F., D. A. Wiens, A. A. Nyblade, S. Anandakrishnan, P. J. Shore, and D. Voigt (2006). Crust and upper mantle structure of the Transantarctic Mountains and surrounding regions from receiver functions, surface waves, and gravity: Implications for uplift models, *Geochem. Geophys. Geosys.* **7**, no. 10, doi: [10.1029/2006GC001282](https://doi.org/10.1029/2006GC001282).
- Lin, F. C., D. Li, R. W. Clayton, and D. Hollis (2013). High-resolution 3D shallow crustal structure in Long Beach, California: Application of ambient noise tomography on a dense seismic array, *Geophysics* **78**, no. 4, Q45–Q56.
- Liu, G., Y. Liu, X. Meng, L. Liu, W. Su, Y. Wang, and Z. Zhang (2021). Surface wave and body wave imaging of passive seismic exploration in shallow coverage area application of Inner Mongolia, *Chin. J. Geophys.* **64**, no. 3, 937–948 (in Chinese).
- Liu, X., B. M. Jahn, Y. Zhao, M. Li, H. Li, and X. Liu (2006). Late Pan-African granitoids from the Grove Mountains, East Antarctica: Age, origin and tectonic implications, *Precambrian Res.* **145**, nos. 1/2, 131–154.
- Liu, X., Y. Zhao, H. Chen, and B. Song (2017). New zircon U–Pb and Hf–Nd isotopic constraints on the timing of magmatism, sedimentation and metamorphism in the northern Prince Charles Mountains, East Antarctica, *Precambrian Res.* **299**, 15–33.
- Liu, X., Y. Zhao, G. Zhao, P. Jian, and G. Xu (2007). Petrology and geochronology of granulites from the McKaskle Hills, eastern Amery Ice Shelf, Antarctica, and implications for the evolution of the Prydz Belt, *J. Petrol.* **48**, no. 8, 1443–1470.
- Liu, Z., X. Tian, R. Gao, G. Wang, Z. Wu, B. Zhou, P. Tan, S. Nie, G. Yu, G. Zhu, et al. (2017). New images of the crustal structure

- beneath eastern Tibet from a high-density seismic array, *Earth Planet. Sci. Lett.* **480**, 33–41.
- O'Donnell, J. P., A. M. Brisbourne, G. W. Stuart, C. K. Dunham, Y. Yang, G. A. Nield, P. L. Whitehouse, A. A. Nyblade, D. A. Wiens, S. Anandakrishnan, *et al.* (2019). The uppermost mantle seismic velocity structure of West Antarctica from Rayleigh wave tomography: Insights into tectonic structure and geothermal heat flow, *Earth Planet. Sci. Lett.* **522**, 219–233.
- Picotti, S., R. Francese, M. Giorgi, F. Pettenati, and J. M. Carcione (2017). Estimation of glacier thicknesses and basal properties using the horizontal-to-vertical component spectral ratio (HVSR) technique from passive seismic data, *J. Glaciol.* **63**, 229–248.
- Ritzwoller, M. H., N. M. Shapiro, A. L. Levshin, and G. M. Leahy (2001). Crustal and upper mantle structure beneath Antarctica and surrounding oceans, *J. Geophys. Res.* **106**, no. B12, 30,645–30,670.
- Shapiro, N. M., M. Campillo, L. Stehly, and M. H. Ritzwoller (2005). High-resolution surface-wave tomography from ambient seismic noise, *Science* **307**, no. 5715, 1615–1618.
- Shiraishi, K., D. J. Dunkley, T. Hokada, C. M. Fanning, H. Kagami, and T. Hamamoto (2008). Geochronological constraints on the Late Proterozoic to Cambrian crustal evolution of eastern Dronning Maud Land, East Antarctica: A synthesis of SHRIMP U-Pb age and Nd model age data, *Geol. Soc. Lond. Spec. Publ.* **308**, no. 1, 21–67.
- Sun, B., J. C. Moore, T. Zwinger, Z. Liyun, D. Steinhage, X. Tang, D. Zhang, X. Cui, and C. Martin (2014). How old is the ice beneath Dome A, Antarctica? *Cryosphere* **8**, no. 3, 1121–1128.
- Sun, B., M. J. Siegert, S. M. Mudd, D. Sugden, S. Fujita, X. B. Cui, Y. Y. Jiang, X. Y. Tang, and Y. S. Li (2009). The Gamburtsev Mountains and the origin and early evolution of the Antarctic ice sheet, *Nature* **459**, no. 7247, 690–693.
- Unrug, R. (1997). Rodinia to Gondwana: The geodynamic map of Gondwana supercontinent assembly, *GSA Today* **7**, no. 1, 1–6.
- Wannamaker, P. E., J. A. Stodt, L. Pellerin, S. L. Olsen, and D. B. Hall (2004). Structure and thermal regime beneath the South Pole region, East Antarctica, from magnetotelluric measurements, *Geophys. J. Int.* **157**, no. 1, 36–54.
- Wilson, T. J., A. M. Grunow, and R. E. Hanson (1997). Gondwana assembly: The view from southern Africa and East Gondwana, *J. Geodyn.* **23**, nos. 3/4, 263–286.
- Wittlinger, G., and V. Farra (2012). Observation of low shear wave velocity at the base of the polar ice sheets: Evidence for enhanced anisotropy, *Geophys. J. Int.* **190**, no. 1, 391–405.
- Wood, W. T., P. L. Stoffa, and T. H. Shipley (1994). Quantitative detection of methane hydrate through high-resolution seismic velocity analysis, *J. Geophys. Res.* **99**, no. B5, 9681–9695.
- Yan, P., Z. Li, F. Li, Y. Yang, W. Hao, and F. Bao (2018). Antarctic ice sheet thickness estimation using the horizontal-to-vertical spectral ratio method with single-station seismic ambient noise, *Cryosphere* **12**, no. 2, 795–810.
- Yao, H., C. Beghein, and R. D. Van Der Hilst (2008). Surface wave array tomography in SE Tibet from ambient seismic noise and two-station analysis—II. Crustal and upper-mantle structure, *Geophys. J. Int.* **173**, no. 1, 205–219.
- Yao, H., R. D. van Der Hilst, and M. V. De Hoop (2006). Surface-wave array tomography in SE Tibet from ambient seismic noise and two-station analysis—I. Phase velocity maps, *Geophys. J. Int.* **166**, no. 2, 732–744.
- Yoshida, M. (1995). Cambrian orogenic belt in East Antarctica and Sri Lanka: Implications for Gondwana assembly: A discussion, *J. Geol.* **103**, no. 4, 467–468.
- Yoshida, M., M. Funaki, and P. W. Vitanage (1992). Proterozoic to mesozoic East Gondwana: The juxtaposition of India, Sri Lanka, and Antarctica, *Tectonics* **11**, no. 2, 381–391.
- Zhan, Z., V. C. Tsai, J. M. Jackson, and D. Helmberger (2014). Ambient noise correlation on the Amery Ice Shelf, East Antarctica, *Geophys. J. Int.* **196**, no. 3, 1796–1802.
- Zhao, Y., X. H. Liu, X. C. Liu, and B. Song (2003). Pan-African events in Prydz Bay, East Antarctica, and their implications for East Gondwana tectonics, *Geol. Soc. Lond. Spec. Publ.* **206**, no. 1, 231–245.

---

Manuscript received 28 May 2021  
Published online 15 September 2021